

In Situ Nanofluid Dispersion Monitoring by Liquid–Solid Triboelectric Nanogenerator Based on Tuning the Structure of the Electric Double Layer

Hao Luo, Hanqing Wang, Lijun Yang, Han Wu, Shenglin Kang, Shun Yong, Ruijin Liao, Jiyu Wang,* and Zhong Lin Wang*

An agglomeration phenomenon characterized by nanoparticle dispersion is a decisive factor that reflects the degree of the maintained overall performance of nanofluids and other nanocomposites. However, the quantitative characterization and non-destructive measurement for nanofluid dispersion (NFD) still remain challenged. Herein, an in situ NFD measurement system based on a variable frequency liquid–solid triboelectric nanogenerator (VFLS-TENG) is developed. This work utilizes VFLS-TENG as a passive probe and proposes an equivalent capacitance circuit model for detecting NFD based on the electric double layer model at liquid–solid interfaces. In the circuit model, a quantitative calculation process for both particle size and spacing is introduced through parameter identification using the Quantum Genetic and Levenberg–Marquardt hybrid algorithm, and parameter separation using the Runge–Kutta algorithm. The results demonstrate a good agreement with the traditional methods, among which the measured particle size is more accurate than the hydrodynamic diameter of dynamic light scattering by 28.6% with a high sensitivity of 1667 nm nF^{-1} . The proposed method is capable of measuring the effective charge on the nanoparticle surface in situ, and simultaneously obtaining the particle size and spacing for the online monitoring NFD, thus further facilitating the controllable preparation during the nano-composites modification, and quantitative optimization of nanofluid design performance.

1. Introduction

Nanofluids are colloidal suspensions by adding nanoparticles in a base liquid with unique features of nano-effects, especially the distinct thermal conductivity, viscosity, and specific heat as heat-transfer dielectrics that are being engineered into transformer oil, turbine lubricants, targets drug carriers, and photothermal conversion medium in various industrial applications.^[1–5] However, the van Der Waals forces between nanoparticles inevitably render themselves prone to agglomeration leading to a significant reduction in the surface effects of nanoparticles, which causes a limitation or even degradation of the overall performance of nanofluids.^[6–8] The nanoparticle dispersion that evaluates the average distance of the nanoparticles in nanofluid is a decisive factor reflecting the degree of the maintained overall performance, which depends mainly on the individual size of the particles and their distributions.^[9–11] In this regard, an effectively quantitative measurement for the particle size distribution of nanoparticles should be proposed for accurately

H. Luo, H. Wang, L. Yang, H. Wu, S. Kang, S. Yong, R. Liao, J. Wang
State Key Laboratory of Power Transmission Equipment
and System Security and New Technology
Chongqing University
Shapingba, Chongqing 400044, P. R. China
E-mail: jiyuwang@cqu.edu.cn

J. Wang
Tsinghua-Berkeley Shenzhen Institute
Tsinghua Shenzhen International Graduate School
Tsinghua University
Shenzhen 518055, P. R. China

Z. L. Wang
Beijing Institute of Nanoenergy and Nanosystems
Chinese Academy of Sciences
Beijing 100083, P. R. China
E-mail: zlwang@binn.cas.cn

Z. L. Wang
CUSPEA Institute of Technology
Wenzhou, Zhejiang 325024, P. R. China

Z. L. Wang
School of Material Science and Engineering
Georgia Institute of Technology
Atlanta, GA 30332, USA

 The ORCID identification number(s) for the author(s) of this article can be found under <https://doi.org/10.1002/adfm.202200862>.

DOI: 10.1002/adfm.202200862

analyzing the degree of particles dispersion in nanofluids to characterize the overall performance of the liquid dielectric.

Previous particle size distribution methods are mostly complicated and still have limitations to achieve in situ and quantitative measurement. The reported measurement methods can be mainly divided into indirect and direct ones. The indirect measurements primarily includes zeta potential method (ZPM) and transmission ratio method (TRM), in which the ZPM is used to evaluate the dispersion stability through the measured zeta potential intensity on the surface of nanoparticles, while the TRM is employed to characterize the dispersion by the absorbance of the suspension. Both methods are only applicable to the specific dispersions with limitations.^[12,13] The direct ones are mainly particle size observation methods, which involves the nanoparticle tracking analysis (NTA), small-angle X-ray scattering (SAXS), scanning electron microscopy (SEM), transmission electron microscopy (TEM), and dynamic light scattering (DLS), etc.^[14] NTA and SAXS are on the principle of light emission to detect particle size with limited detection concentration and range.^[15,16] The SEM and TEM are able to achieve the high resolution particle size and spacing, though both of them can capture only partial characteristics. More importantly, such measurements require a great number of statistic information to evaluate the overall dispersion, still have a long distance to the in situ measurement. In addition, the DLS based on the light scattering principle to obtain the particle size distribution curve in a quick calculation, but its optical detection is subject to several interference factors, and the spacing of particles are still unattainable.^[17–19] In fact, although the surface charge amount, particle size and spacing of nanoparticles can be obtained separately with current methods, the different procedures for sampling preparations may impair the original properties of these particles, bringing about inaccuracy in the final synthesis.^[20] Thus, a new method for in situ and quantitative measurement of nanofluid dispersion (NFD) is still worthy of further research.

Notably, as the electric double layer model of nanoparticles firstly proposed by Lewis et al. was universally convincing, the distribution of nanoparticles therefore can be regarded as a series of capacitances, paving ways for the calculations of the particle size and their spacing by the capacitance variation to obtain the dispersion.^[21] However, the test circuits composed of conventional power supply are mostly resistive, which are not easily reconcilable with capacitive loads. More importantly, the transfer charge amount of the power supply is uncontrollable and random in circuit, making the parameters of capacitance hard to be quantitatively identified. Recently, triboelectric nanogenerators (TEGs) based on the coupling of triboelectrification and electrostatic induction were widely reported as distinctive detection probes with fixed generated charge quantity that applied into the particle quality characterization, mass spectrometric characterization, electron trap state characterization, induced interface spectroscopy etc.^[22–26] These research were mostly focused on the solid–solid interfaces, while the NFD detection relied on the liquid–solid TENG (LS-TENG), which once proved having a comparable perception but has not been reported yet as a detection probe.^[27,28] On one hand, the LS-TENG owns merits of wear resistance and durability, also can output more stable signal for the better flexibility

and fluidity of liquids, and maintain higher sensitivity with its encapsulation isolated to the external ambients.^[29,30] Moreover, the newly proposed Wang's hybrid layer model by Wang et al. has elaborated the potential distribution and changing rules of the generated charges at liquid–solid contact interface, settling the quantization problem of the transferred charges in the parameters identification for the NFD analysis.^[31,32] Meanwhile, Wang et al. demonstrates that the output characteristics of LS-TENG are influenced by the dielectric properties of various liquids,^[33] which offers an idea that the nanofluid can also be filled in as a liquid dielectric, whose dielectric properties will alter with the change of NFD according to the electric double layer theory.^[21,34] In this case, the LS-TENG has the potentials of being designed as a probe for the NFD detection.

Herein, an in situ NFD measurement system based on a variable frequency liquid–solid TENG (VFLS-TENG) is reported, and the electric double layer model at liquid–solid interfaces is also proposed for the nano-agglomeration characterizations. In this work, the VFLS-TENG device consisting of fluorinated ethylene propylene (FEP) tube and copper electrodes was designed into a tubular structure with variable frequency feature for the broadened output spectrum. The equivalent capacitance circuit model is proposed by measuring the output signals of SiO₂ and ZnO at different volume fractions and ultrasonic times with the electric double layer model of nanoparticles. The specific equivalent capacitance value of each particle was calculated after the overall and local optimizations through the Quantum Genetic and Levenberg–Marquardt hybrid algorithm (QLHA), and the average particle size and spacing were further separated iteratively by using Runge–Kutta algorithm (RKA). Unlike previous reports, this method can precisely quantify the equivalent capacitance particle size of nanoparticles, which is nearer to the geometric particle size with higher accuracy than the hydrodynamic diameter measured by DLS. Moreover, the proposed method has the capability to characterize the effective charge amount on the surface of nanoparticles in situ, and further to obtain the particle size and spacing of nanoparticles simultaneously, whose result merges the advantages of direct and indirect measurements, and even bridges the relationship between the direct and indirect ones. This work provides a non-destructive and effective strategy to extract nano-agglomeration parameters from the equivalent capacitance and charged quantities of particles probed by TENGs based on an electrical double layer model at the liquid–solid interfaces, which offers a novel method for quantitative detection of NFD.

2. Results and Discussion

2.1. Structure and Working Mechanism of LS-TENG

As shown in **Figure 1a**, the LS-TENG probe-based measurement system for monitoring NFD is mainly composed of a peristaltic pump used for driving the nanofluid, and an LS-TENG as the core of the measurement system. The peristaltic pump was chosen as an auxiliary device to absorb the pending nanofluid solutions prepared at different volume fractions and ultrasonic times, and make them steadily flow through the LS-TENG to achieve the stable signal. The LS-TENG herein has

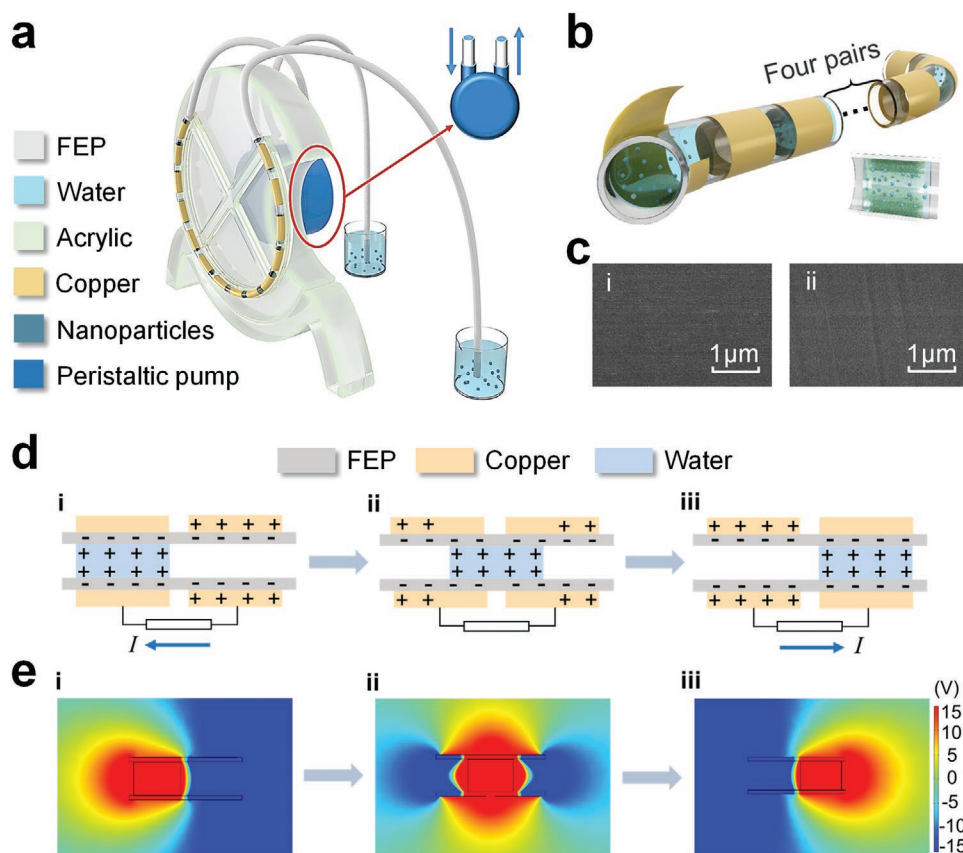


Figure 1. Structure and mechanism of the LS-TENG probe-based measurement system for monitoring NFD. a) Detailed structure of a detection system combining an LS-TENG with a peristaltic pump, where a peristaltic pump is utilized to realize the entrance and egress of nanofluid into and out of the LS-TENG. b) Schematic diagram of LS-TENG with an extended cross-sectional view of a 7-pair electrode, which clearly shows the nanoparticles dispersed in deionized water. c) Comparison of SEM images for FEP inner tube wall i) before and ii) after three-month operation. d) Schematic diagram of the charge distribution and current direction of the LS-TENG during the whole cycle (i–iii). e) Potential distribution simulated by COMSOL employing the finite element method at the corresponding displacements (i–iii).

three parts: an FEP tube as the structural framework, copper films used as electrodes, and the internal filled nanofluid solution as the fluid-state dielectrics. The FEP is selected as the triboelectric material for the excellent electronegativity, favorable flexibility, and hydrophobic characteristics.^[35,36] The LS-TENG is mounted on a base of an acrylic plate with double-crossed acrylic spokes supporting its inner periphery to hold the stability under operations. As the LS-TENG expanded in Figure 1b, the cross-sectional view of solution with nanoparticles can be clearly observed. Here, the LS-TENG is designed in two electrode terminals with 7 pairs of electrodes, of which the adjacent electrodes belong to opposite terminals, and the inner solution will be divided into section by the intermittent extraction to only overlap the same terminals at one time. Figure 1c(i,ii) shows the SEM images of the FEP-tube inner surface before and after three months of operations, and the comparison reveals that the inner surface of the FEP-tube hardly produces any frictional scratches under repeated sliding friction during three months, whose preferable wear resistance and durability are mainly contributed to the distinct feature of the liquid-dielectric based TENG. Notably, due to the fact that the influence of the absorption effect of nanoparticles on the inner wall is minimal especially in the transient processes, meanwhile, the TENG

measurement method is fast and nondestructive, the possible absorption of the particle on the wall could be neglected.

As the peristaltic pump is activated, the nanofluid in the beaker will be pumped into the LS-TENG, and the corresponding signal will be generated due to the coupling effect of triboelectrification and electrostatic induction, in which the flowing liquid inside the FEP tube will cause the generation of triboelectric charges and the transfer of induced positive charges subsequently. Figure 1d illustrates the electricity generation process of LS-TENG in detail. In the initial state, after sufficient contact between the inner surface of the FEP-tube and the injected liquid, triboelectric effect will cause the negative charges on the inner surface of tube, and an equal amount of the positive charges in the liquid. When the liquid flows, the induced positive charges accordingly transferred, leading to the potential difference due to the asymmetric charge amount between the left and right electrodes, thus drives electrons flow from one electrode to the other through an external circuit, where the current is generated. In state (i), as the positively charged liquid covers the left electrode of the FEP tube, which results in almost no charge generation on the copper electrode on the left, while a large positive charge accumulates around the copper electrode on the right. As the liquid flows to the

right side, lying between the left and right electrodes at state (ii), the potential difference is 0. When the liquid fully covers the right electrode, the opposite potential difference will be established, where the whole cycle of electricity generation by the LS-TENG is finished. To further understand the working mechanism of the LS-TENG, the continuous variation of the open circuit voltage V_{oc} is demonstrated by COMSOL finite element simulation, as shown in Figure 1e. V_{oc} is defined as the potential difference between the left and right electrodes, when the negative charge on the inner surface of the FEP tube is sequentially shielded by the positive charge from the flowing liquid, a potential difference will be generated due to the electrostatic induction. Therefore, the maximum absolute value of V_{oc} will occur in stage (i) and stage (iii), where the flowing liquid fully covers the copper electrode, and the negative charge on the FEP-tube is completely shielded by the positive charge in liquid. As the liquid flows, the V_{oc} will gradually decrease because the liquid will help to shield the triboelectric charge on both sides of the electrodes during the flow (ii). Once the liquid position is exactly in the center of the left and right electrodes, the same charge on both sides is precisely equal and no potential difference is generated, where the V_{oc} is 0.

2.2. Structural Exploration of the LS-TENG

In the structural optimization of LS-TENG, the FEP tube with an inner diameter of 4 mm is selected considering the connection of peristaltic pump, and deionized water is firstly utilized as the flowing fluid. Since the LS-TENG is employed as a perception sensor for NFD detection, which imposes a certain signal-to-noise ratio requirement on the output signal, thus the relevant parameters including the liquid length, copper electrode length, interval length of adjacent electrodes were discussed on the influence rules of the waveform distortion rate and output power. As illustrated in Figure 2a, based on the electricity generation principle of the freestanding mode of the TENG,^[37] when the length of copper electrode is given as L , the length of sliding liquid in the tube is optional to be set at the value of single electrode length or the total length between the two ends of the left and right electrodes. Besides, the output of LS-TENG is also affected by the interval length between the left and right electrodes, thus the interval can be represented as L/N , where the N is taken as 1, 2, 4, 8. For the liquid length optimization, five TENG structures with copper electrode length L varying from 2 to 6 cm at which the interval length is set at L ($N = 1$) were fabricated, and the driven liquid lengths were L and $3L$, whose output peak power curves with varied external load resistances in Figure S1, Supporting Information. Figure 2b exhibits the maximum power density for the liquids at the L and $3L$ lengths calculated by the varied copper electrode length, in which the power density at the same electrode length is about three times higher for the length L than that for the length $3L$, and the power density at both liquid lengths shows an uptrend and then downtrend with the increase of the copper electrode length, both achieve the maximum value at 5 cm. The reason for the difference can be attributed to the frequency difference of the output current produced from the TENG, and ultimately influence the output power.

For the interval length between electrodes, 20 TENGs whose copper electrode length L varied from 2 to 6 cm with the interval length according to the variation of N were crafted, and the respective output voltages curves are shown in Figure S2, Supporting Information. As shown in Figure 2c, with the increase of the copper electrode length, the output voltage shows an uptrend. While at the same electrode length, with the decrease of the interval length, the voltage basically remains constant as the interval length reduces. Therefore, it is difficult to directly confirm the optimal length of copper electrode by one indicator of the amplitude of the output voltage.

Besides the output voltage as one of the evaluation index, the distortion rate of the signal waveform should be further calculated to determine the structural parameters. Here, the maximum value of the fast Fourier transform (FFT) processing method is utilized as the fundamental frequency to calculate the total harmonic distortion rate (THD) at the 5th harmonic and 10th harmonic.^[38] Its fundamental frequency calculation formula is denoted as Equation (1).

$$f = \frac{1}{T} = \frac{v}{L + \frac{L}{N}} \quad (1)$$

where T is a complete power generation cycle, v is the flow rate of the liquid, which is also one of the main factors affecting the output, but owing to excessive flow rate, the water in the tube will be further dispersed causing an extended covering area that overlaps with two adjacent electrodes, so the flow rate in this work is controlled in the peristaltic pump adjustable button 30% of the drive speed, about 1.33 cm s^{-1} .

After the signal of the output voltage processed by the FFT, the formula about THD is shown in Equation (2).

$$THD = \frac{\sqrt{U_2^2 + U_3^2 + U_4^2 + \dots + U_n^2}}{U_1} \times 100\% \quad (2)$$

where U_1 is the rms value of the fundamental voltage, U_2 is the rms value of the second harmonic voltage, and similarly, U_n is the rms value of the n th harmonic voltage.

The output signals under the 20-group structures were processed by FFT and their THD values were calculated with the results shown in Figure 2d. It can be seen that under the 5th harmonic, the overall waveform distortion rate value of each interval length is relatively small when $L = 4$ and 5 cm, indicating that the output is more stable with the maximum distortion rate value less than 10%. This rate increases slightly even under the 10th harmonic (Figure S3, Supporting Information), so that the copper electrode length L should be considered as 4 or 5 cm.

Moreover, the relationship between the load resistance and the output peak power under $L = 4$ and $L = 5$ can be observed in Figure 2e,f. The maximum output power of $L = 4$ cm increases about 5 times from $N = 1$ to $N = 8$ at a load resistance of $10 \text{ M}\Omega$, which is similar to the trend of $L = 5$ cm. Herein, for $L = 5$ cm, only 1 mL water can produce a maximum power of 0.0069 mW at $N = 8$. But for practical applications, not only the output power is required to be large, but also the threshold width of the load response is required to be as wide as possible. Hence,

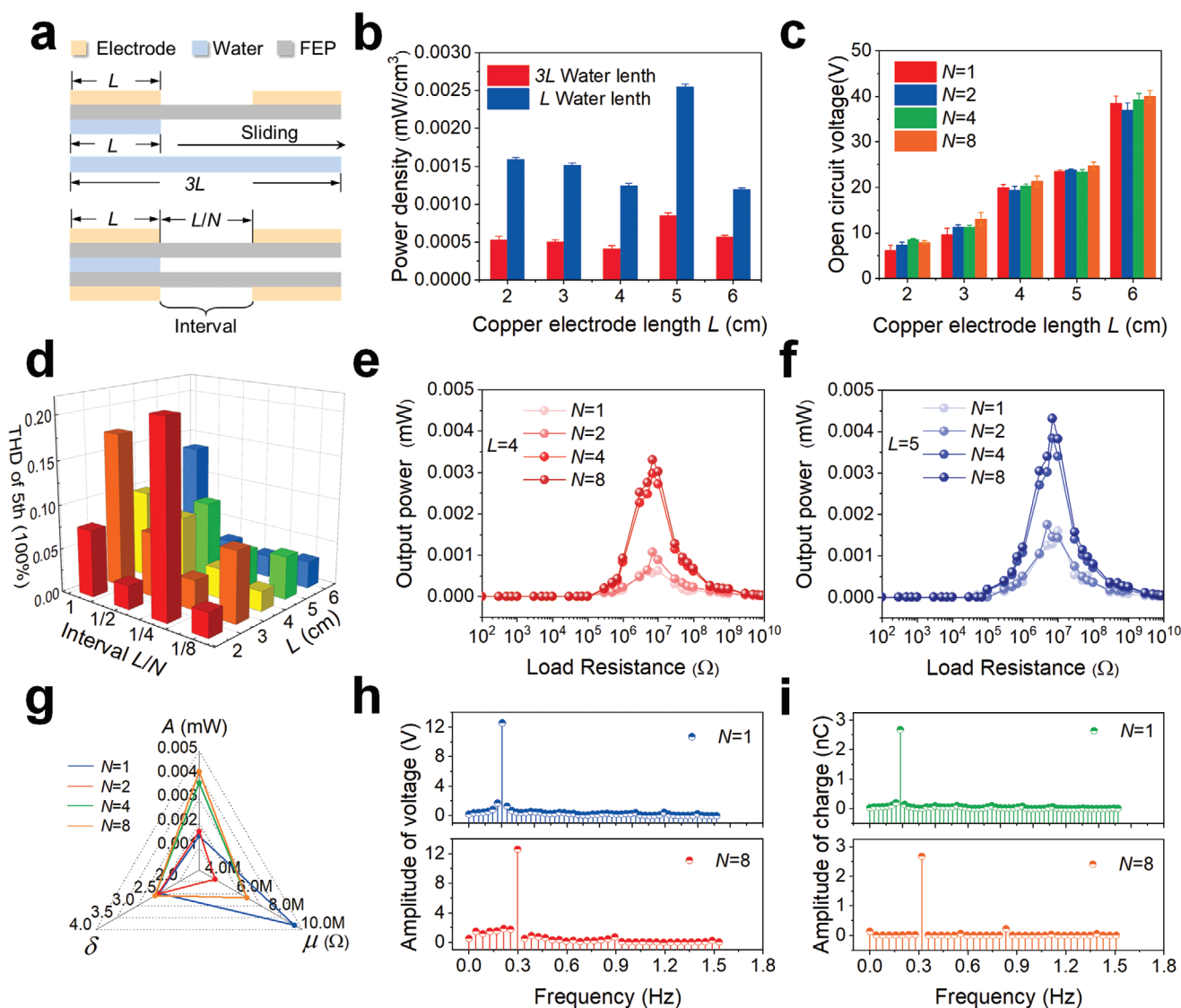


Figure 2. Exploration of structural parameters for original LS-TENG. a) Schematic diagram of the lengths of copper electrode, liquid dielectric, and interval. b) Comparison of the power density of two water column drives at the same copper electrode length. c) Measured relationship between different interval and output voltage with the same copper electrode length. d) Calculated the THD at different copper electrode lengths and different intervals. Output peak power with external load resistance at different intervals for copper electrode lengths of e) 4 and f) 5 cm. g) Triangular plot of power amplitude, threshold width, and external load resistance with different intervals for copper electrode length of 5 cm. Spectral amplitude information of h) output voltage and i) transferred charge at different intervals.

the data of matching resistance and output power are fitted into a normal distribution curve in this work, whose three parameters of probability density function are calculated, and the formula is given by Equation (3).

$$f(x) = A \frac{(x - \mu)^2}{\delta} \quad (3)$$

where A is the amplitude of the output peak power, μ is the external load resistance, and δ is the threshold width of the load response.

By comparing the three parameters between $L = 4$ and $L = 5$ in Figure 2g, it is found that the output peak power and threshold width at $L = 5$ cm are better than those at $L = 4$ cm (Figure S4,

Supporting Information). Thus, the copper electrode length $L = 5$ cm was finally determined in this work with the consideration of output voltage, output power, THD value, and load response threshold width. As shown in Figure 2h,i, the spectrum of FFT was analyzed for each interval under the copper electrode length $L = 5$ cm, and it was revealed that although the output power was increased at $N = 8$, there was basically no difference in the voltage amplitude and charge output, but only a certain frequency difference existed for different interval lengths. As a result, a single interval length variation has limitations for subsequent analysis of the capacitive circuit model of nanoparticles, and further improvements are needed to integrate into a new VFLS-TENG for the more sensitive NFD detection.

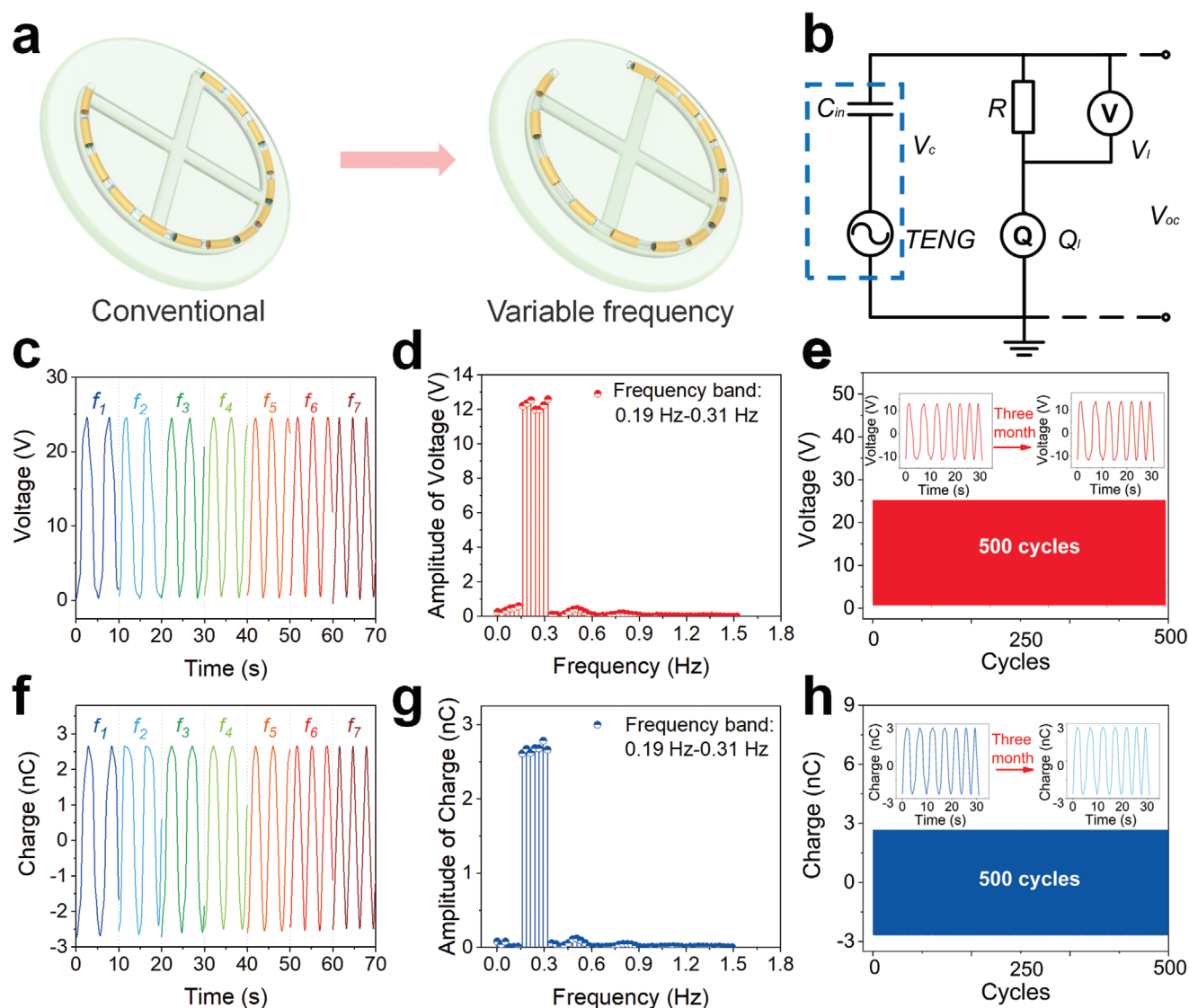


Figure 3. Electrical output performance of the improved VFLS-TENG. a) Schematic diagram of the VFLS-TENG. b) The internal capacitance C_{in} test circuit of the VFLS-TENG. The open-circuit voltage V_{oc} , and f) transfer charge Q_I in different frequencies at 7 pairs of electrodes. Spectrum amplitude of d) V_{oc} , and g) Q_I under the VFLS-TENG. Comparison of e) V_{oc} and h) Q_I before and after the VFLS-TENG is placed at ambient temperature for 3 months.

2.3. The Improved VFLS-TENG and its Output Performance

For further enriching the spectrum information of output signal, and facilitating the theoretical analysis on the parameters identification, a modified alterable frequency structure is proposed. As shown in **Figure 3a**, the original symmetric structure with equal interval is evolved into an asymmetric structure with the interval length varied from $L/1$ to $L/8$ consecutively (Photograph and structure design are displayed in Figure S5, Supporting Information). In this case, the settled liquid flow rate can produce frequency-varying signals, which is conducive to the spectral analysis after FFT. As connected with external measuring circuit in **Figure 3b**, parameters identification of nanofluid can be obtained by the signals of the open-circuit voltage (V_{oc}), the load voltage (V_I), the transferred charge (Q_I), and the voltage across the internal capacitor of the nanofluid

(V_c), that is, $V_c = V_{oc} - V_I$. The matched resistance here is taken as $R = 10M\Omega$ (**Figure 2f**), corresponding to the maximum output power for the favorable resolution. As depicted in **Figure 3c–e**, the VFLS-TENG outputs signals with seven different frequencies in one single cycle, whose V_{oc} remains constant at about 25 V. According to Equation (1), the frequency range can be derived at 0.19–0.31 Hz, whose spectrum information is more abundant compared with that in **Figure 2h**. Meanwhile, the durability of the VFLS-TENG was also verified, and the voltage signal keeps constant after about 500 continuous cycles due to the good encapsulation. Notably, this work also compares the original output signal with that after three months, finding the output only fluctuates by about 5%, which represents a preferable durability of the device. Similarly, the charge output has similar characteristic in **Figure 3f–h**, the transferred charge Q with seven different frequencies in one single cycle

remains constant at about 2.67 nC, in which the spectrum data information becomes 7 times larger than the original one, and also demonstrates favorable durability.

2.4. Sample Preparation and Detection of TENG-NFD Measurement System

To establish the equivalent capacitance circuit model, two types of nanofluids with varied configurations as samples were prepared to obtain the output signals for the parameters identification. Figure 4a presents the flow chart of nanofluid preparation, in which 50 mL deionized water and specific amount of nanoparticles (SiO_2 and ZnO) are mixed up to obtain the nanofluids with different volume fractions (0.01%, 0.03%, 0.05%, 0.1%, 0.15%), then ultrasonic shaking was performed for different times (0 min, 15 min, 30 min, 60 min) to form the tested nanofluid samples. Owing to the different volume fraction and ultrasonic time, the particle size of two types of nanoparticles varied accordingly, which in turn triggers different surface and size effects thus eventually lead to different macroscopic dielectric properties.^[34] Here we take the 0.01% volume fraction, for example, the SEM images of SiO_2 and ZnO samples in the same volume fraction but different ultrasonic time were obtained, with the results of 30 min shown in Figure 4b,c, and others can be referred in Figure S6, Supporting Information. It can be visually observed that these two samples are better dispersed at 30 min, and the SEM results of different times reveal the positive correlation between the NFD and the ultrasonic time. Besides, it was found that the SiO_2 particles were spheroidal particle that would be fitted with the electric double layer model, while the ZnO particles were in the bulk shape which needed to be approximately treated as the spherical shape for the calculation of bilayer capacitance. And the results of the particle size distribution curve, zeta potential, and conductivity measured by DLS used to characterize the dispersion illustrate similar trend under ultrasonic times, as shown in Figure S7, Supporting Information. For instance, the zeta potential and conductivity of two types of nanofluids were exhibited in Figure 4d, where the absolute values of zeta potential for both are greater than 30 mV, indicating a preferable stability of the two nanofluids after the ultrasonic time of 15 min.^[39,40] In addition, it is worth noting that the conductivity of the measured samples were all $317 \mu\text{S}$, which stays unchanged with the increase of ultrasonic time, demonstrating that the equivalent of the electric double layer of nanoparticles is not a resistive load but a capacitive one, laying the foundation for the capacitive circuit model.

In the equivalent capacitance circuit model, the internal capacitance of VFLS-TENG needs to be firstly obtained by testing the voltage and charge output of the nanofluid samples. Figure 4e,f illustrates that the output voltage V_c of SiO_2 nanofluid at the same volume fraction gradually rises with the increase of ultrasonic time, but the transfer charge Q_t shows a downward tendency. It is due to the fact that as the dispersion becomes progressively better with increasing sonication time, polarization occurs at the interface between nanoparticles and water, which increases the relative permittivity of the nanofluid and eventually leads to the enhancement of the output voltage. Meanwhile, the particle size of nanoparticles

gradually reduces as the dispersion becomes better, which causes a decrease in the particle equivalent capacitance and ultimately results in a drop in the internal capacitance. Since the decreasing tendency of internal capacitance is dominant, thus the transferred charge shows a downward trend with the increase of sonication time, the details are given in Note S1, Supporting Information. Moreover, the output voltage of SiO_2 nanofluid as a liquid dielectric in TENG shows an overall trend that first increases then slightly decreases with the growth of volume fraction at a certain ultrasonic time, while the transferred charge shows an overall trend of initially reducing then increasing. Correspondingly, the output waveforms for the SiO_2 nanofluids are shown in Figure S8, Supporting Information, the output voltage and transfer charge waveforms of each sample possess different frequencies in one cycle, which facilitates the enrichment of information in the spectrum data. In general, it can be observed that the output signal varies significantly under each sample, which is due to the difference in sample dispersion at different states. Therefore, the internal capacitance C_{in} can be directly obtained from the spectral data of V_c and Q_t . For example, taking a sample of SiO_2 with a volume fraction of 0.01% in different ultrasonic times, Figure 4g exhibits the variation of C_{in} with frequency, whose values are obtained from the calculation of the FFT. It is found that there is a maximum value at the fundamental frequency and decreases gradually with frequency. Moreover, it is also observed that the overall C_{in} reduces with the rise of ultrasonic time. Thus it illustrates that although the trends of output voltage and transferred charge are different, the variation of the internal capacitance is regular which gradually reduces as the ultrasonic treatment time increases from 0 to 60 min. The C_{in} results for the remaining SiO_2 nanofluid samples are given in Figure S9, Supporting Information. Figure 4h,i shows the V_c and Q_t of the ZnO nanofluid, in which the trend of V_c experiences a first sharp increase and a slight decrease afterward with the increment of ultrasonic time at the volume fractions of 0.01–0.05%, whose maximum voltage output occurs at 30 min. As the volume fractions raises up to 0.1–0.15%, the V_c gradually increases and achieves the maximum output value at 60 min, indicating that the lower sample concentration requires less time for a better dispersion. Similarly, the transfer charge Q_t still shows a downward tendency with the increase of ultrasonic time. And the waveforms about the output voltage and transferred charge of the ZnO sample are depicted in Figure S10, Supporting Information. Figure 4j is the C_{in} results of the ZnO samples with the volume fraction of 0.01%, which is consistent with the tendency of the SiO_2 samples. (The C_{in} measurement results for the remaining ZnO nanofluid samples are given in Figure S11, Supporting Information. Overall, it was found that the C_{in} measured for different samples varies with ultrasound time, resulting in different sizes but maintaining a similar tendency. Based on electric double layer theory, it is due to the different sizes and distributions of particles in water. So in order to identify the size and distribution of particles, this work needs to further refine the C_{in} , an equivalent circuit model based on the electric double layer theory at the liquid–solid interface is established for the NFD detection.

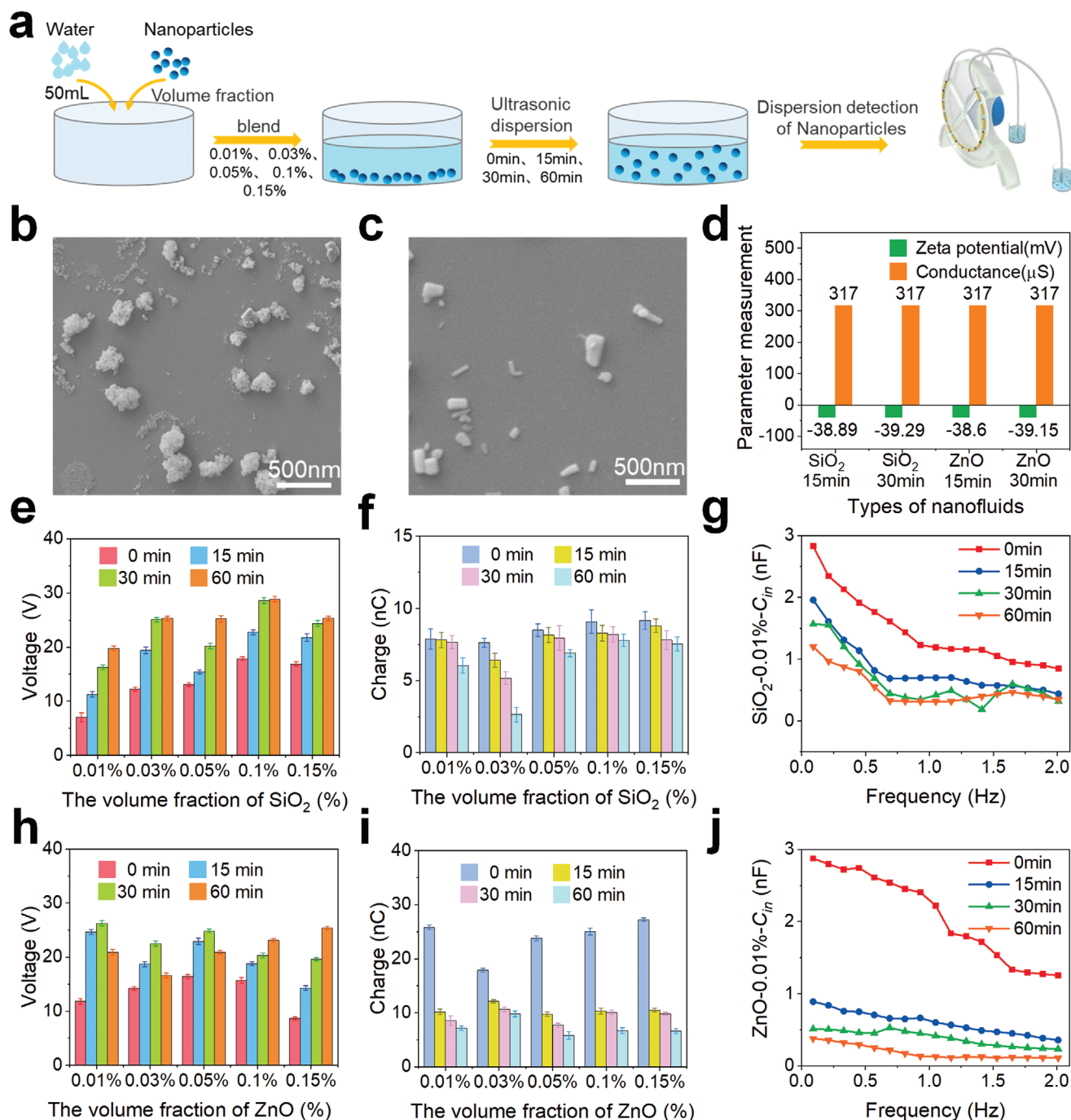


Figure 4. Sample preparation and detection of TENG-NFD measurement system. a) Flow diagram of the nanofluid formulation. SEM images of b) SiO₂ and c) ZnO nanofluid at volume fraction 0.01% and ultrasonic time 30 min. d) Zeta potential and conductivity tested at different nanofluid samples with 0.01% volume fraction. Variation of e) V_c and f) Q_I of SiO₂ nanofluid with increasing ultrasonic time at each volume fraction. g) C_{in} measurement results at different ultrasonic times for SiO₂ sample with volume fraction of 0.01%. Variation of h) V_c and i) Q_I of ZnO nanofluid with increasing ultrasonic time at each volume fraction. j) C_{in} measurement results at different ultrasonic times for ZnO sample with volume fraction of 0.01%.

2.5. Modeling and Analyzing of TENG-NFD Measurement System

The measured internal capacitance C_{in} in the above nanofluid samples by VFLS-TENG has been found an overall downward tendency with the increased sonication time, which is due to

the different dispersion degrees that are intrinsically correlated with the dielectric properties. To specifically characterize the dielectric property for the better identifications of the particle size distribution and spacing range of particles in nanofluids, this work combines the liquid–solid electric double layer model proposed by Wang et al.^[31] and the electric double layer

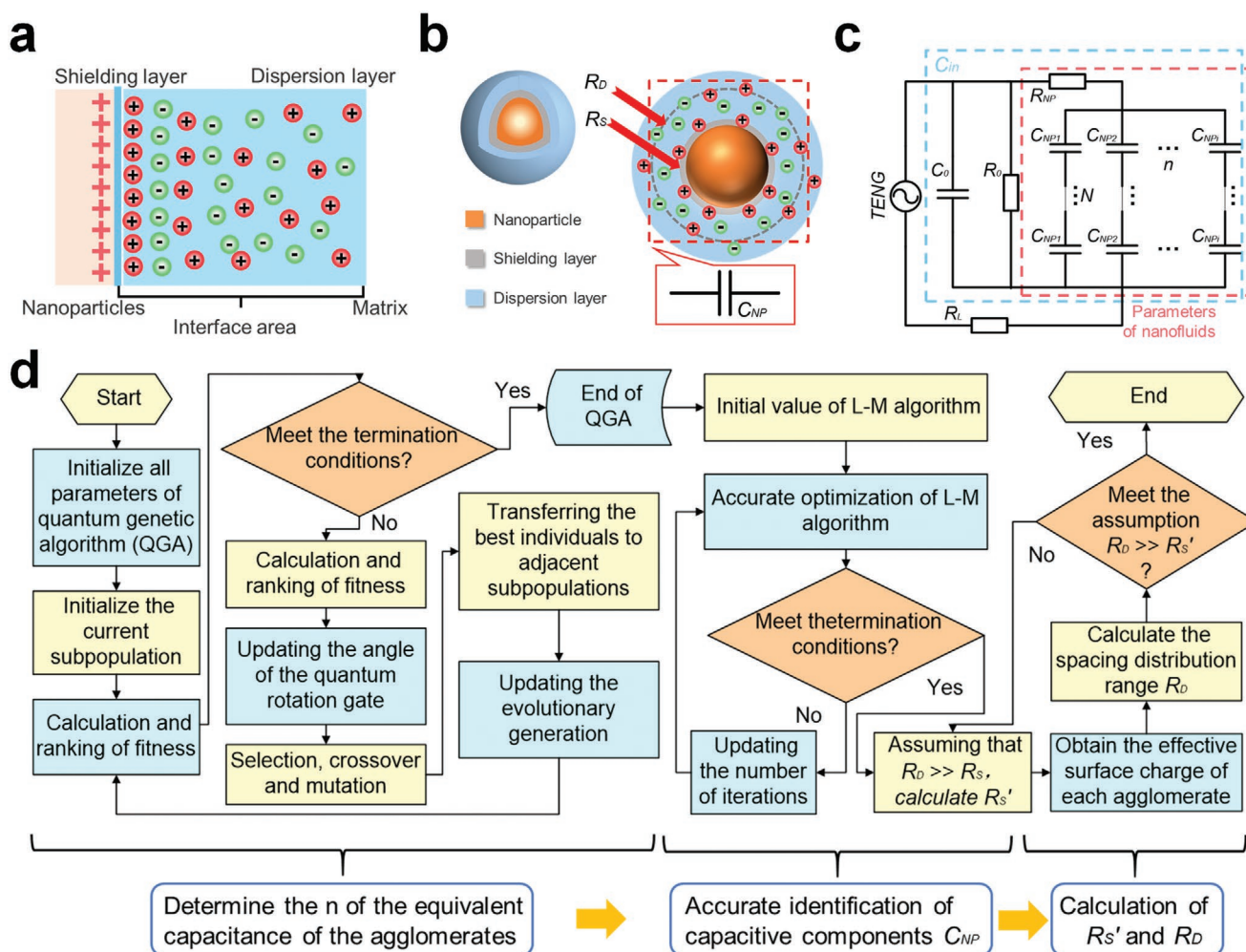


Figure 5. Equivalent capacitance circuit model and algorithm solution for TENG-NFD measurement system. a) Schematic diagram of liquid–solid contact electrification and formation of electric double layer. b) Double layer structure profile of nanoparticles. c) Equivalent capacitance circuit model for identifying the parameters of nanofluid, the blue square is the internal capacitance of TENG, and the red square is the circuit parameters of nanofluid. d) Optimization algorithms and separation algorithms for extracting particle size and spacing by calculating the equivalent capacitance in nanofluids.

theory of nanoparticles from Lewis et al.,^[21] then extend them into the nanofluid field. In this way, the equivalent capacitance C_{NP} of nanoparticles can be deduced from the electric double layer model, and an equivalent capacitance circuit model representing the NFD system can also be established, in which the C_{NP} is largely influenced by the particle size and spacing distribution of the particles. In **Figure 5a**, as the liquid contacts the virgin solid surface, the overlap of electron clouds causes electrons to transfer at the liquid–solid interface, and the ionization reaction occurs simultaneously on the solid surface, therefore the ions with opposite charges in the liquid will be attracted to migrate toward the charged surface by electrostatic interaction, forming a liquid–solid electric double layer.^[41] Meanwhile, the charged particles in the liquid will migrate and diffuse due to Coulomb forces, and an electric double layer structure is also formed around the nanoparticles. As the electric double layers of neighboring particles in the nanofluid overlap with each other, the charge transfer mechanism inside the liquid medium accordingly alters, turning out to affect the macroscopic dielectric properties of the nanofluid.^[34] Moreover, the distribution of

nanoparticles can also be regarded as a series of capacitances, so the relationship between the dielectric properties of the electric double layer and the particle size as well as the particles spacing can be characterized by C_{NP} ,^[42–45] as illustrated in Equation (4).

$$C_{NP} = \frac{4\pi\epsilon_l R_s R_D}{(R_D - R_s)} \quad (4)$$

where C_{NP} is the equivalent capacitance value of nanoparticle agglomerates, ϵ_l is the dielectric constant of the liquid, R_s is the geometric radius of the nanoparticles, R_D is the cutoff radius of the dielectric layer that can be regarded as spacing. As illustrated in **Figure 5b** and Equation (4), with the increased degree of particle agglomeration, the particle size R_s increases, and the spacing R_D increases as well, which eventually leads to the variation of C_{NP} . The deduction process for the equivalent capacitance of the electric double layer structure is presented in Note S2, Supporting Information. In addition, the previous studies on LS-TENG have demonstrated that the contact

electrification between the liquid dielectric and the solid electrode can be equally explained by the electric double layer model of the liquid–solid interface.^[41,46,47] Therefore, the C_{in} parameter measured in Figure 4g,j comprises the equivalent capacitance C_0 of the VFLS-TENG and the C_{NP} of the nanofluid system. As above, the overall equivalent circuit model is established in Figure 5c. For the equivalent circuit model with n branches, the solution details are given in Note S3, Supporting Information, and the internal capacitance C_{in} of the VFLS-TENG can be expressed by Equation (5).

$$C_{in} = \frac{1}{j\omega Z} = C_0 - j \frac{1}{\omega R_0} + \frac{\sum_{i=1}^n \frac{C_{NPi}}{N_i} \left(1 - j\omega R_{NP} \left(\sum_{i=1}^n \frac{C_{NPi}}{N_i} \right) \right)}{1 + \left(\omega R_{NP} \left(\sum_{i=1}^n \frac{C_{NPi}}{N_i} \right) \right)^2} \quad (5)$$

According to Equation (5), the real part $C'(\omega)$ and imaginary part $C''(\omega)$ of the internal capacitance C_{in} can be derived as Equations (6) and (7).

$$C'(\omega) = C_0 + \frac{\sum_{i=1}^n \frac{C_{NPi}}{N_i}}{1 + \left(\omega R_{NP} \left(\sum_{i=1}^n \frac{C_{NPi}}{N_i} \right) \right)^2} \quad (6)$$

$$C''(\omega) = \frac{1}{\omega R_0} + \frac{\omega R_{NP} \left(\sum_{i=1}^n \frac{C_{NPi}}{N_i} \right)^2}{1 + \left(\omega R_{NP} \left(\sum_{i=1}^n \frac{C_{NPi}}{N_i} \right) \right)^2} \quad (7)$$

C_{in} is the internal capacitance of the VFLS-TENG, C_0 is the geometric equivalent capacitance of the FEP tube, ω is the angular frequency, R_0 is the internal resistance of the FEP tube, and C_{NPi} is the type i agglomerate equivalent capacitance. Since the equivalent resistance of the nanofluid R_{NP} is much smaller than R_0 , and the conductivity of the nanofluid remains unchanged in the DLS measurement, so it can be neglected in the circuit identification process. N_i is the series order of equivalent capacitance of the class i agglomerate, which is proportional to the relative content of class i agglomerates whose content indicates the number of nanoparticle monomer within the agglomerates. Moreover, the structure of the electric double layer is tuned due to the addition of nanoparticles, which causes changes in the circuit parameters, the details are given in Note S4, Supporting Information.

So far, an equivalent circuit model based on the electrical double layer structure at the liquid–solid interface is established, and the inner parameters in the C_{in} measurement results have also been analyzed. This circuit model not only contains the capacitance C_0 of the VFLS-TENG and the capacitance C_{NP} of the nanofluid, but also clarifies the relationship between nano-agglomerate scale, particle size R_S and spacing R_D with C_{NPi} and N_i . For further quantifying NFD, it is necessary to separate R_S and R_D through the C_{NP} and the measured surface charge of the particles. As expressed in Equations (6) and (7), since the real and imaginary parts of the internal capacitance C_{in} are

relevant to C_{NPi} and N_i , therefore the $C'(\omega)$ and $C''(\omega)$ in the C_{in} can be taken as the reference data for parameter identification. It can thus be seen that the parameter identification of this circuit model is a multi-parameter nonlinear fitting problem, which can be solved by transforming into a multi-parameter nonlinear optimization model. In this regard, the least squares method is utilized to establish the optimization objective function f , as described in Equation (8), which ensures that the error between the actual measurement value and the model calculation value of C_{in} is minimized.

$$f = \min \left[\sum_{i=1}^m (C'_{Actual}(\omega) - C'_{Model}(\omega))^2 + \sum_{i=1}^m (C''_{Actual}(\omega) - C''_{Model}(\omega))^2 \right] \quad (8)$$

Where $C'_{Actual}(\omega)$ and $C''_{Actual}(\omega)$ are the actual measured values of real and imaginary parts, $C'_{Model}(\omega)$ and $C''_{Model}(\omega)$ are the corresponding model calculated values. The optimal solution sets of N_i and C_{NPi} that satisfy the requirements of the electric double-layer equivalent circuit model can be obtained by iterative calculations of $C'_{Model}(\omega)$ and $C''_{Model}(\omega)$ based on Equations (6) and (7) when the objective function f converges to the minimum value of 0.

For any optimization goals from high-dimensional nonlinear function, the solution process is more demanding on the initial value selection and convergence ability of the algorithm. In order to avoid the large dependence on initial value, this work adopts the QLHA algorithm to settle the parameter identification in optimization model.^[48,49] As shown in Figure 5d, the global optimization is first performed with Quantum Genetic algorithm (QGA) to determine the circuit order n , and initially tighten the feasible domain, then Levenberg–Marquardt algorithm is utilized to achieve the exact local optimization search in the feasible domain given by QGA to derive the parameter identification results of C_{NP} . In addition, for further separation of the particle size R_S and spacing R_D from C_{NP} , this work initially assumes that R_D is much larger than R_S , so that the particle size value R'_S can be obtained preferentially. Next, the total charge of nanoparticles under each sample is calculated from the experimental measured transfer charge of nanofluids and pure water. Then, the transfer charge of each agglomerate is attained from the total charge of nanoparticles and the particle size distribution of R'_S . Finally, based on the theory proposed by Derjaguin, Landau and Verwey, Overbeek (DLVO), the spacing R_D is calculated from the particle size and surface charge of the agglomerates^[50–54] and is modified iteratively with RKA. The details are described in Note S5, Supporting Information. During the above calculation, C_{in} was obtained from the measured spectral information of V_c and Q , varying with the nanofluid sample, C_0 was measured by the Lenz capacitor resistance meter (Solartron 1260) to be 20 mF, and both R_0 and R_L were taken to the maximum matching load impedance value of 10 M Ω in the circuit (Figure 2f).

As demonstrated in Figure 6a, taking the SiO₂ sample with a volume fraction of 0.01% as an example, it is observed that the similarity between the actual measured values and the model calculated values of C_{in} at different ultrasonic times is basically around 95%, which indicates that the C_{NP} results identified by this equivalent circuit model have a good agreement and conformity. The actual measured values of C_{in} under different

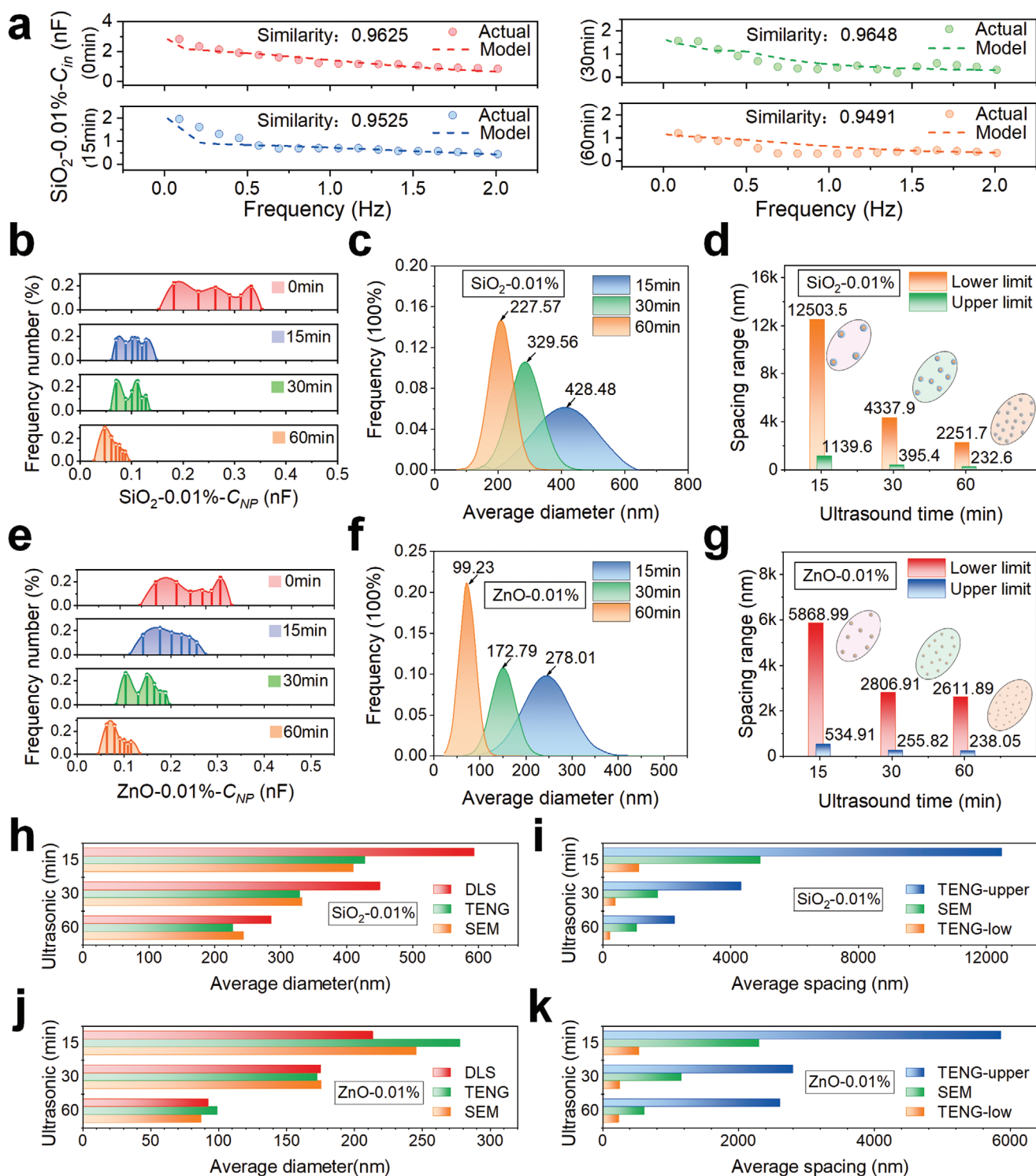


Figure 6. Parameter identification and separation results of the TENG-NFD measurement system. a) Similarity between the actual measured and model-calculated values of C_{in} at different ultrasound times. b) Identification results of C_{NP} , c) Average particle size distribution curve, and d) Average spacing at different sonication times for SiO_2 with volume fraction of 0.01%. e) Identification results of C_{NP} , f) Average particle size and g) average spacing at different sonication times for ZnO with volume fraction of 0.01%. Comparison of h) average particle size and i) average spacing of three measurement methods at different ultrasound times for SiO_2 with volume fraction of 0.01%. Comparison of j) average particle size and k) average spacing of three measurement methods at different ultrasound times for ZnO with volume fraction of 0.01%.

samples maintain a high similarity to the model calculated values are shown in Figure S12, Supporting Information. In this work, the values of C_{NP} are obtained based on their respective equivalent circuit model and the optimal objective function with the results in Figure 6b,e. Figure 6b shows that the C_{NP} decreases continuously with the increase of sonication time, and each type of nanoparticle agglomerate occupies a different proportion. The C_{NP} results contain both particle size and spacing information that were further separated under the iteration of RKA. The particle size distribution curve of nanofluids shifts to the left with the increased ultrasonic time as illustrated in Figure 6c, and the average particle sizes are quantitatively calculated as 428.48 and 227.57 nm at 15 and 60 min, respectively. Furthermore, we also calculated the average particle spacing based on the particle size distribution and the particle surface charge. The spacing shows a gradually decreasing trend with the growth of the sonication time in Figure 6d. The reason for the fact is that the total volume of nanoparticles stays constant in the same sample, the number of particles increases as the dispersion gradually becomes better, which results in a naturally shorter distance between particles. The average spacing can be quantified from 1139.6 nm to 12 503.5 nm at 15 min, and it becomes 232.6 nm to 2251.7 nm at 60 min. For another, there is a similar variation tendency with the SiO_2 sample for the ZnO nanofluid with a volume fraction of 0.01% as indicated in Figure 6e–g, the average particle size and spacing are also quantitatively obtained at different ultrasound times.

Finally, to verify the accuracy of the characterization method for quantitatively measuring the NFD, the above TENG-NFD measurement results are compared with the results of DLS and the statistical results of SEM in Figure 6h–k. For the SiO_2 sample with a volume fraction of 0.01%, the three measurement methods basically exhibit similar tendencies in Figure 6h. It is worth noting that there is a higher deviation observed in the DLS measurement results, which is owing to the fact that the DLS results are the hydrodynamic diameter including an additional layer of aquifer. On the contrary, the results of both TENG-NFD measurement system and SEM are consistent with each other. Here taking the SEM measurement results as the reference standards, the particle size measured by TENG-NFD measurement system shows a 28.6% higher accuracy than that measured from DLS, whose sensitivity also reaches up to 1667 nm nF^{-1} . Notably, the results from the DLS measurements are based on the assumption that the measured nanoparticles are spherical, and the temperature is set at room temperature during the measurement, which is similar to the TENG-NFD measurement method. For both methods, the results of the DLS and TENG-NFD are not contradictory, but simply represent the two particle size results which are the hydrodynamic diameter and the equivalent particle size. For the spacing measurements, since the DLS cannot obtain the spacing of the particles, herein the spacing results from the TENG-NFD measurement system are compared with the average spacing from SEM as shown in Figure 6i. It is observed that the upper and lower limits of the average spacing measured by TENG-NFD measurement system exactly cover the average spacing of the SEM measurement results. Likewise, Figure 6j displays a comparison of the results of the three measurement methods under ZnO nanofluid, and the general tendency is similar to

that of the SiO_2 sample. However, the DLS results at 15 min show lower results, which can be attributed to the reason that although the DLS measurement results are hydrodynamic diameters, there is also a bias towards small or large particles due to the measurement angle.^[14] Thus, the DLS results in Figure 6j may be biased towards small particles resulting in lower results. Accordingly, as revealed in Figure 6k, it indicates that the upper and lower limits of the average spacing measured by TENG-NFD measurement system under ZnO nanofluid still achieves well agreement with the SEM results, indicating the applicability to substitute the SEM as a novel method for the particles spacing measurement. Details of the particle size for the measurement results of DLS and SEM in the above samples are shown in Figure S13, Supporting Information, and the average particle spacing measured by SEM is illustrated in Figures S14 and S15, Supporting Information. Overall, the above description proves the feasibility of the TENG-NFD measurement system applied to quantitative measurement of NFD, which solves the high deviation and unattainable spacing results of DLS, while avoiding the destructive tests of traditional methods, thus achieving a favorable applicability. Moreover, the pH conditions and temperature of the liquid phase environment will be further considered in future work. Therefore, the TENG-NFD measurement system with the improved variable frequency structure is potentially regarded as a sensitive, quantitative, low-cost, and nondestructive test method for particle size and spacing of nanofluids, while the charged quantity of particles can be captured by the in situ testing process. This TENG-based method can break through the shortcomings of the existing methods that cannot simultaneously characterize nanoparticle size, dispersion spacing, and effective charge of particles, which can greatly increase the accuracy of controllable preparation during the nano-composites fabrication and modification, paving ways for the quantitative optimization of nanofluid design performance under multi-physics field.

3. Conclusion

In summary, an NFD measurement system based on the VFLS-TENG for the in situ and quantitative characterization of nano-agglomeration is proposed in this work. Nanofluids like SiO_2 and ZnO particles with different dispersions as liquid dielectric exhibit different dielectric properties that can be perceived by VFLS-TENG with a good sensitivity. The output characteristics of different volume fractions, ultrasonic times, and particle types of various nanofluid samples were measured by utilizing VFLS-TENG to obtain the internal capacitance C_{in} . Besides, an equivalent capacitance circuit model is then established, which is conducive to clarify the nanoparticle dispersion in nanofluids based on an electrical double layer model at the liquid–solid interface. On this basis, the parameter identification by QLHA and the parameter separation by RKA were proposed to quantify the average particle size and spacing of nanoparticle agglomerates. The results of the TENG-NFD measurement system have been proved with a good agreement and conformity with existing methods, and its accuracy for NFD detection were also demonstrated with the measurement results of DLS and SEM. Referring to the SEM results,

the measured particle size of TENG-NFD measurement system is more accurate than that of DLS by a percent of 28.6, with a high sensitivity of 1667 nm nF^{-1} . The proposed method enables in situ detection of the effective charge on the nanoparticle surface and obtains the particle size and spacing, simultaneously. For this work, the effects of electrolytes and organic solvents or gas bubbles will be further considered in our future work and quantified by subsequent experimental corrections for this proposed circuit model. The TENG-NFD measurement system features self-powered characteristics and swift accuracy, which has the potential to be directly applied to in situ and quantitative online monitoring of nanoparticle dispersion in nanomaterial synthesis processes. Furthermore, it can be further applied in controllable preparation to analyze nanofluids performance under multi-physics field by providing key parameters in a one-off way for quantitative calculations of multi-scale processes like colloidal phase transition and flow heat transfer.

4. Experimental Section

Fabrication of TENGs: The main part of TENG is made of 4 mm thick inner diameter FEP tube with very high polarity and transparency, as shown in Figure 1b. The FEP tube was first truncated to a specified length (about 104 cm) and the two end ports have the same inner diameter for the peristaltic pump interface, which facilitates the cyclic experiment after connection. Moreover, 7 pairs of conductive copper strips (5 cm) with adhesive backing were orderly decreasing according to the interval ratio of 1 to 8, where each interval was gradually reduced in step of 0.4 cm and pasted to the surface of the FEP tube to form the variable frequency multi-gate structure. For experimental studies, the electrode length can be adjusted to the desired length (2, 3, 4, 5, and 6 cm), and the length of the liquid dielectric was ensured to be the same as the length of the copper electrode. In addition, the TENG was mounted on the base of an acrylic plate, and then a cross was adhered to the inner circumference and a ring of supporting spokes was adhered to the periphery to fix the tubular TENG. Where the adjacent copper electrodes were opposite electrodes and the segments were cross-connected, and the liquid dielectric was made to circulate through the VFSL-TENG device using the drive of a peristaltic pump.

Preparation of Nanofluid: 50 mL of deionized water and specific amounts of nanoparticles (SiO_2 and ZnO) were mixed into beakers to prepare nanoparticle solutions with different volume fractions (0.01%, 0.03%, 0.05%, 0.1%, 0.15%), and then ultrasonic cell crusher was used for different times (0 min, 15 min, 30 min, 60 min) and finally, the nanofluid samples of different features were obtained.

Electrical Measurements: To evaluate optimal performance, the open circuit voltage and transfer charge of the TENG device were measured by a Keithley 6514 system electrostatics meter. The measurement signals were input high-speed data acquisition system under LabView control.

Statistical Analysis: To measure the particle size, a conventional ImageJ software was utilized to calculate the particle size manually for the SEM images. Firstly, the image was opened with TIFF format by ImageJ, and then the plotted lines were overlapped with the scale length to complete the scale setting. Second, the diameter of a particle was marked by utilizing the line drawing tool, and then the measurement tool was clicked to measure the nanoparticle size data, where the particle size statistics were extracted from at least 100 nanoparticles. Herein, the statistics were mainly combined with multiple electron micrographs in the same sample, and not repeated to ensure accuracy. Finally, the data were saved as an xls file and plotted using Origin to show the mean and standard deviation of the particle size distribution. For the average spacing statistics of particles, the radial distribution function was introduced in this manuscript as the basis for the statistical inter-particle distance. The radial distribution of particles at different locations in

each sample was obtained by varying the value of the micro-radius dr (200–8000 nm), and the highest probability dr at each position was then determined as the average spacing of the particles within the nanofluid.

Supporting Information

Supporting Information is available from the Wiley Online Library or from the author.

Acknowledgements

H.L. and H.W. contributed equally to this work. This work was supported by the National Natural Science Foundation of China (Grant No. 52007019).

Conflict of Interest

The authors declare no conflict of interest.

Data Availability Statement

The data that support the findings of this study are available from the corresponding author upon reasonable request.

Keywords

electric double layers, liquid–solid triboelectric nanogenerators, nanofluid dispersion, self-powered systems

Received: January 21, 2022

Revised: March 7, 2022

Published online:

- [1] S. U. S. Choi, J. Eastman, *ASME Int. Mechanical Engineering Congress & Exposition*, San Francisco, CA **1995**.
- [2] N. S. Suhaimi, M. Faiz, M. Din, T. Ishak, J. Wang, *Sci. Rep.* **2020**, *10*, 8.
- [3] L. Rapoport, Y. Bilik, *Nature* **2012**, *387*, 791.
- [4] T. Yong, X. Zhang, N. Bie, H. Zhang, X. Zhang, F. Li, A. Hakeem, J. Hu, L. Gan, H. A. Santos, *Nat. Commun.* **2019**, *10*, 3838.
- [5] D. Mateo, N. Morlanes, P. Maity, G. Shterk, O. F. Mohammed, J. Gascon, *Adv. Funct. Mater.* **2021**, *31*, 2008224.
- [6] M. Mackay, A. Tuteja, P. Duxbury, C. Hawker, B. Van Horn, Z. Guan, *Science* **2006**, *311*, 1740.
- [7] N. M. Kovalchuk, D. J. Johnson, V. Sobolev, N. Hilal, I. Voicu, *Adv. Colloid Interface Sci.* **2019**, *272*, 102020.
- [8] R. Wang, S. Qian, Z. Zhang, *Int. J. Heat Mass Transfer* **2018**, *127*, 1138.
- [9] K. Suttiponpanit, J. Jiang, M. Sahu, S. Suvachittanon, T. Charinpanitkul, P. Biswas, *Nanoscale Res. Lett.* **2011**, *6*, 27.
- [10] P. Koblinski, J. A. Eastman, D. G. Cahill, *Mater. Today* **2005**, *8*, 36.
- [11] D. Cressey, *Nature* **2010**, *467*, 264.
- [12] A. Gupta, S. Vasudevan, *J. Phys. Chem. C* **2018**, *122*, 19243.
- [13] G. Bickert, W. Stahl, *Part. Part. Syst. Charact.* **1997**, *14*, 142.
- [14] N. I. Anaraki, A. Sadeghpour, K. Iranshahi, C. Toncelli, A. Neels, *Nano Res.* **2020**, *13*, 2847.
- [15] K. Guo, J. Liu, *China Powder Sci. Technol.* **2014**, *20*, 41.

- [16] T. Li, A. J. Senesi, B. Lee, *Chem. Rev.* **2016**, *16*, 11128.
- [17] M. Ste Fa Nos, P. R. Molto, T. Kim, *Nanoscale* **2018**, *10*, 12871.
- [18] B. Lee, S. Yoon, J. W. Lee, J. H. Lee, *ACS Nano* **2020**, *14*, 17125.
- [19] R. Sharma, *Micron* **2012**, *43*, 1147.
- [20] C. R. Li, *Journal of Sun Yat-sen University: Natural Science Edition* **2005**, *44*, 3.
- [21] J. T. Lewis, *IEEE Trans. Dielectr. Electr. Insul.* **1994**, *1*, 812.
- [22] S. Lin, Z. L. Wang, *Appl. Phys. Lett.* **2021**, *118*, 193901.
- [23] L. Wang, J. Li, J. Tao, M. Hu, Z. Dai, *Nano Energy* **2021**, *89*, 106393.
- [24] Y. Li, M. Bouza, C. Wu, H. Guo, F. Fernandez, *Nat. Commun.* **2020**, *11*, 5625.
- [25] H. Wang, J. Wang, R. Liao, L. Yang, H. Wu, Z. L. Wang, *Adv. Funct. Mater.* **2021**, *31*, 2103463.
- [26] D. Li, C. Xu, Y. Liao, W. Z. Cai, Y. Q. Zhu, Z. L. Wang, *Sci. Adv.* **2021**, *7*, eabj0349.
- [27] X. Zhang, M. Yu, Z. Ma, H. Ouyang, Y. Zou, S. L. Zhang, H. Niu, X. Pan, M. Xu, Z. Li, *Adv. Funct. Mater.* **2019**, *29*, 1900327.
- [28] X. Li, L. Zhang, Y. Feng, Y. Zheng, Z. Wu, X. Zhang, N. Wang, D. Wang, F. Zhou, *Adv. Funct. Mater.* **2021**, *31*, 2010220.
- [29] W. Tang, T. Jiang, F. R. Fan, A. F. Yu, X. Cao, Z. L. Wang, *Adv. Funct. Mater.* **2015**, *25*, 3718.
- [30] S. Chatterjee, S. Saha, S. R. Barman, I. Khan, Z. H. Lin, *Nano Energy* **2020**, *77*, 105093.
- [31] F. Zhan, A. C. Wang, L. Xu, S. Lin, Z. L. Wang, *ACS Nano* **2020**, *14*, 17565.
- [32] Z. Tang, S. Lin, Z. L. Wang, *Adv. Mater.* **2021**, *33*, 2102886.
- [33] J. Wang, Z. Wu, L. Pan, R. Gao, B. Zhang, L. Yang, H. Guo, R. Liao, Z. L. Wang, *ACS Nano* **2019**, *13*, 2587.
- [34] M. P. Ahmad, A. V. Rao, K. S. Babu, G. N. Rao, *Mater. Chem. Phys.* **2019**, *224*, 79.
- [35] C. Cai, B. Luo, Y. Liu, Q. Fu, T. Liu, S. Wang, S. Nie, *Mater. Today* **2021**, *51*, 155.
- [36] L. Pan, J. Wang, P. Wang, R. Gao, Y. C. Wang, X. Zhang, Z. L. Wang, *Nano Res.* **2018**, *11*, 4062.
- [37] X. Li, T. H. Lau, D. Guan, Y. Zi, *J. Mater. Chem. A* **2019**, *7*, 24691.
- [38] M. F. Wahab, F. Gritti, T. C. O'Haver, *TrAC, Trends Anal. Chem.* **2021**, *143*, 116354.
- [39] A. Ozs, C. Ratb, A. An, *Phys. Rep.* **2020**, *867*, 1.
- [40] H. Farzaneh, A. Behzadmehr, M. Yaghoubi, A. Samimi, S. M. H. Sarvari, *Energy Convers. Manage.* **2016**, *111*, 1.
- [41] S. Lin, L. Xu, A. C. Wang, Z. L. Wang, *Nat. Commun.* **2020**, *11*, 399.
- [42] J. Wang, S. R. MacEwan, A. Chilkoti, *Nano Lett.* **2017**, *17*, 1226.
- [43] K. Bohinc, G. V. Bossa, S. May, *Adv. Colloid Interface Sci.* **2017**, *249*, 220.
- [44] R. Warmbier, N. Malaza, A. Quandt, *Ionics* **2017**, *23*, 331.
- [45] S. Zhang, Z. Zhang, S. Chen, R. Zhu, *Anal. Chem.* **2021**, *93*, 5882.
- [46] S. Lin, X. Chen, Z. L. Wang, *Chem. Rev.* **2022**, *122*, 5209.
- [47] M. Sun, Q. Lu, Z. L. Wang, B. Huang, *Nat. Commun.* **2021**, *12*, 1752.
- [48] L. Du, F. Yang, C. Wei, Y. Wang, L. Ran, *Transactions of China Electro-technical Society* **2018**, *33*, 1158.
- [49] L. Yang, J. Chen, S. Wang, J. Gao, *IEEE Trans. Dielectr. Electr. Insul.* **2018**, *25*, 1688.
- [50] X. Zhang, Y. E. Chunsong, X. Jia, T. Liu, J. Huang, *Thermal Per Generation* **2018**, *47*, 48.
- [51] D. U. Xuan, X. U. Sheng-Hua, Z. W. Sun, A. A. Yan, *Acta. Phys. Chim. Sin.* **2010**, *26*, 2807.
- [52] H. T. Wang, Y. N. Dong, M. Zhu, X. Li, A. A. Keller, T. Wang, F. T. Li, *Water Res.* **2015**, *80*, 130.
- [53] X. Mu, D. Wang, T. Feng, C. Kübel, *Microsc. Microanal.* **2016**, *22*, 488.
- [54] G. MASON, *Nature* **1968**, *217*, 733.